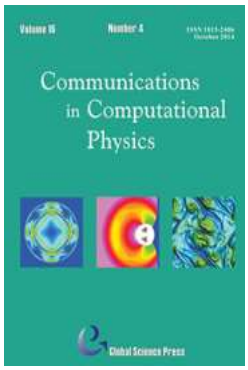

An Immersed Interface Method for Axisymmetric Electrohydrodynamic Simulations in Stokes flow

H. Nganguia, Y.-N. Young, A. T. Layton, W.-F. Hu and M.-C. Lai

Communications in Computational Physics / Volume 18 / Issue 02 / August 2015, pp 429 - 449
DOI: 10.4208/cicp.171014.270315a, Published online: 30 July 2015

Link to this article: http://journals.cambridge.org/abstract_S1815240615000651

How to cite this article:
H. Nganguia, Y.-N. Young, A. T. Layton, W.-F. Hu and M.-C. Lai (2015). An Immersed Interface Method for Axisymmetric Electrohydrodynamic Simulations in Stokes flow. Communications in Computational Physics, 18, pp 429-449 doi:10.4208/cicp.171014.270315a

Commun. Comput. Phys.
doi: 10.4208/cicp.171014.270315a

Vol. **18**, No. 2, pp. 429-449
August 2015

An Immersed Interface Method for Axisymmetric Electrohydrodynamic Simulations in Stokes flow

H. Nganguia[1,2], Y.-N. Young[2,*], A. T. Layton[3], W.-F. Hu[4] and M.-C. Lai[4]

[1] *Department of Biological Sciences, New Jersey Institute of Technology, Newark, NJ 07102, USA.*
[2] *Department of Mathematical Sciences, New Jersey Institute of Technology, Newark, NJ 07102, USA.*
[3] *Department of Mathematics, Duke University, Box 90320, Durham, NC 27708, USA.*
[4] *Department of Applied Mathematics, National Chiao Tung University, 1001, Ta Hsueh Road, Hsingchu 300, Taiwan, R.O.C.*

Received 17 October 2014; Accepted (in revised version) 27 March 2015

Abstract. A numerical scheme based on the immersed interface method (IIM) is developed to simulate the dynamics of an axisymmetric viscous drop under an electric field. In this work, the IIM is used to solve both the fluid velocity field and the electric potential field. Detailed numerical studies on the numerical scheme show a second-order convergence. Moreover, our numerical scheme is validated by the good agreement with previous analytical models [1, 31, 39], and numerical results from the boundary integral simulations [17]. Our method can be extended to Navier-Stokes fluid flow with nonlinear inertia effects.

AMS subject classifications: 76W05, 65M06, 65M12

Key words: Immersed interface method, least squares interpolation, electrohydrodynamics.

1 Introduction

Under a direct current (DC) electric field an electrohydrodynamic flow is induced both inside and around a viscous drop [28, 37, 39]. Depending on the electrical properties of the fluids the viscous drop can deform into a prolate (oblate) spheroid with its major axis parallel (perpendicular) to the electric field. Such electrohydrodynamics of a viscous drop has a wide range of applications in micro-fluidic systems [36, 45], from drop manipulation by electro-wetting [6] to enhanced mixing inside and on a drop in a Stokes

*Corresponding author. *Email addresses:* hn9@njit.edu (H. Nganguia), yyoung@njit.edu (Y.-N. Young), alayton@math.duke.edu (A. T. Layton), weifanhu.am95g@g2.nctu.edu.tw (W.-F. Hu), mclai@math.nctu.edu.tw (M.-C. Lai)

flow [2, 11, 32, 44]. Several theoretical models and numerical schemes have been developed to study the drop dynamics under a DC electric field. Theoretical studies are often restricted to nearly spherical [1, 39, 42] or spheroidal shapes [4, 31, 46]. Consequently these models can only capture the drop electrohydrodynamics up to a moderate electric field, and cannot predict the extreme drop elongation, lobed steady drop shape and several break-up modes under a strong DC field observed in experiments [13, 14] and direct numerical simulations. Various numerical schemes have been developed to simulate electrohydrodynamic (EHD) flow with certain limitations. For example, the boundary integral method [7, 17, 38] cannot be easily extended to different configurations such as solving the full Navier-Stokes equations, or accounting for charge effects in the bulk fluid. Sharp methods such as the ghost-fluid method [33, 35] are generally first-order accurate. Tomar *et al.* [41] used the volume of fluid (VOF) method, where jumps in electrical and fluid properties across the drop interface are smoothed out in a transition region around the moving interface. A direct consequence of the smoothing is the reduction in the order of accuracy. The finite element method [10] is too computationally expensive for deforming/moving interfaces.

To investigate the electrodeformation of a viscous drop with inertia effects (finite Reynolds number), recently Hu *et al.* [15] developed a hybrid numerical scheme, using the immersed boundary (IB) method for the incompressible Navier-Stokes flow (finite Reynolds number) and the augmented immersed interface method (AIIM) for the electric potential. The authors treated the electric Maxwell stress as an interfacial force to facilitate a unified immersed boundary framework, and illustrated first-order convergence for the electric force calculations. In addition this code can efficiently simulate large drop deformation under both an electric field and a shear flow.

Based on results in [15], we have developed an immersed interface method (IIM) for axisymmetric electrohydrodynamics of a viscous drop in the present study. Both the electric and the fluid equations are solved within the immersed interface framework with axisymmetry. The fluid solver is based on an axisymmetric immersed interface algorithm [24]. The electric solver is an AIIM modified from [15] to account for the axisymmetry of the drop interface.

The IIM was initially developed to solve elliptic equations with discontinuous coefficients and/or singular sources [20]. The basic idea behind the IIM is to modify the finite difference discretization of the discretized governing equations near irregular grid points by adding correction terms that depend on the boundary conditions at an interface. The IIM differs from the immersed boundary method (IB method) [34], another popular method for solving similar problems, in that the IIM does not regularize the singular forces at the interface. Instead, it captures the interfacial discontinuity in a sharp manner, and yields a second-order convergence rate. While second-order IB methods exist [5, 12, 19, 30], the second-order accuracy is reduced to first order for problems that involve an infinitely sharp interface [29], such as the drop interface that we consider here. Therefore in this work we use IIM with consistent order of accuracy (second-order) for both the electric field and the fluid flow. In addition, our IIM algorithm is developed for

an axisymmetric viscous drop in three dimensions.

The paper is organized as follows: The problem formulation and governing equations are presented in Section 2. The numerical methods for both the fluid and electric components are described in Section 3. The IIM to solve the electric potential in axisymmetric coordinates is developed in Section 3.1, and the implementation of the IIM for the flow field is presented in Section 3.2. Finally, the convergence analysis and comparison against analytical models (such as the spheroidal model [31]) and boundary integral numerical simulation results [17] are discussed in Section 4.

2 Problem formulation

A schematic diagram of the problem formulation is shown in Fig. 1: an initially spherical viscous drop under a DC field $\boldsymbol{E}_0$, whose direction is parallel to the axis of symmetry. The interface Γ separates the exterior fluid (superscript '+' for the exterior domain Ω^+) from the interior fluid (superscript '-' for the interior domain Ω^-).

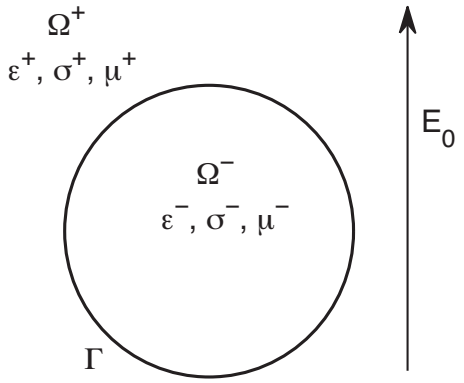

Figure 1: Sketch of the problem: A leaky dielectric viscous drop (in domain Ω^-) immersed in another dielectric fluid (in domain Ω^+), with an external electric field E_0 in the z direction. Subscript '+' and '-' denote the exterior and interior fluids, respectively.

Within each subdomain, the fluid flow is described by the incompressible Stokes equation

$$-\nabla p^j + \mu^j \nabla^2 \boldsymbol{u}^j = 0, \tag{2.1}$$

$$\nabla \cdot \boldsymbol{u}^j = 0, \tag{2.2}$$

where $j = '+'$ for the exterior fluid and $j = '-'$ for the interior fluid. $p, \boldsymbol{u} = (u, w)$ and the parameter μ denote the pressure, flow field, and fluid viscosity, respectively. In the bulk the electric permittivity ε^j and conductivity σ^j may be different between the exterior ('+') and interior ('-') of the drop. The ratios of permittivities and conductivities are defined

as

$$\varepsilon_r = \frac{\varepsilon^-}{\varepsilon^+} \equiv Q, \qquad \sigma_r = \frac{\sigma^-}{\sigma^+} \equiv \frac{1}{R}, \tag{2.3}$$

where Q and R are notations used in [17]. For convenient comparison to boundary integral results in [17], we use (Q, R) instead of $(\varepsilon_r, \sigma_r)$ when we present our IIM simulation results in Section 4.

The drop interface Γ is given in parametric form $\boldsymbol{X}(s,t) = (\rho(s,t), Z(s,t))$, where the parameter $0 \le s \le 2\pi$. $(\rho(s,t), Z(s,t))$ are the polar coordinates of the interface Γ in the r and z directions, respectively. Under an external electric field, bulk charges neutralize instantaneously in the leaky dielectric framework [28], and consequently the electric potential ϕ satisfies the Laplace equation

$$\nabla \cdot (\varepsilon \nabla \phi) = 0, \tag{2.4}$$

with the far-field boundary condition $\nabla \phi^+ = -\boldsymbol{E}_0 \hat{\boldsymbol{z}}$, and the boundary conditions on the drop interface

$$[\![\phi]\!] = 0, \qquad [\![\sigma \nabla \phi \cdot \boldsymbol{n}]\!] = \frac{d\tilde{q}}{dt}, \tag{2.5}$$

where $\boldsymbol{n}$ is the unit outward normal, $\tilde{q} = [\![\varepsilon \nabla \phi \cdot \boldsymbol{n}]\!]$ represents the surface charge density, and $[\![\cdot]\!]$ denotes the jump between outside and inside quantities. For "weakly" conducting dielectric fluids, the charging time $t_c \equiv \varepsilon^j / \sigma^j$ is much faster than the time scale $t_{EHD} = \mu^j / \varepsilon^j E_0^2$ of the electrohydrodynamic flow in most applications: $t_c \ll t_{EHD}$. Therefore the charge convection term on the right hand side of Eq. (2.5) is often ignored in the leaky dielectric framework [9], and the jump condition on the normal electric field reduces to $[\![\sigma \nabla \phi \cdot \boldsymbol{n}]\!] = 0$.

The electric force $\boldsymbol{F}_E$ is related to the Maxwell stress $\mathbf{M}$ as $\boldsymbol{F}_E = \nabla \cdot \mathbf{M}$, and $\mathbf{M}$ is computed from the electric field $\boldsymbol{E}$ as

$$\mathbf{M} = \varepsilon \left(\boldsymbol{E}\boldsymbol{E} - \frac{1}{2} E^2 \mathbf{I} \right), \tag{2.6}$$

where $\mathbf{I}$ is the identity tensor. In the leaky dielectric formulation, the electric force is important only when there is a gradient or jump in the electrical conductivity σ and/or permittivity ε. As these electrical properties are assumed to be piecewise constant with a possible jump across the drop interface in our formulation (see Fig. 2), the electric force $\boldsymbol{F}_E$ can be treated as an interfacial force given by the jump in Maxwell stress in the normal direction, as done in the boundary integral method [27].

At the drop interface the stress balance gives

$$\left(-p^+ + p^-\right) \mathbf{n} + [\![\mathbf{T}^{hd}]\!] \cdot \mathbf{n} + \boldsymbol{f} = 0, \tag{2.7}$$

where $(\mathbf{T}^{hd})_{ij} \equiv \mu(\partial_i u_j + \partial_j u_i)$ is the ij-th component of the viscous stress tensor, and $[\![\cdot]\!]$ denotes the difference between exterior and interior fluids. The traction $\boldsymbol{f}$ consists of the

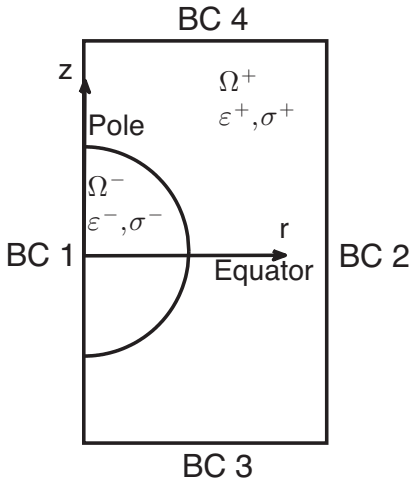

Figure 2: Computational domain on the (r,z)-plane. See text for the boundary conditions. On the walls BC 1, 2, 3, and 4 denote the boundary conditions defined in Eqs. (3.1)-(3.4).

surface tension [8, 18] and electric force, and is given by

$$\boldsymbol{f}=\boldsymbol{f}_\gamma+\boldsymbol{f}_E=\gamma\left(\frac{\rho_s Z_{ss}-\rho_{ss}Z_s}{|\boldsymbol{X}_s|^3}+\frac{Z_s}{\rho}\right)\boldsymbol{n}+[\![\mathbf{M}\cdot\boldsymbol{n}]\!], \tag{2.8}$$

where γ is the surface tension along the drop interface $\boldsymbol{X}=(\rho,Z)$, and $|\boldsymbol{X}_s|=\sqrt{\rho_s^2+Z_s^2}$, with the subscript 's' denoting partial derivatives with respect to the Lagrangian parameter s.

3 Numerical methods

The governing equations in Section 2 are cast in cylindrical coordinates (r,z) for our axisymmetric system (Fig. 2), and the velocity field $\boldsymbol{u}=(u,w)$. These equations are solved over the $r\geq 0$ half-plane and then extended to the left half-plane $r<0$ by symmetry. We denote Δt as the time step size and $t_n=n\Delta t$ as the nth time-level with $n=0,1,2,\cdots$. At a time level t_n, the position of the drop interface is given by a set of (N_B+1) Lagrangian markers, $\mathbf{X}=(\rho_k^n,Z_k^n)$ for $k=0,1,2,\cdots,N_B$, with $k=0$ at the north pole and $k=N_B/2$ at the south pole. The drop is immersed in the domain $\Omega=[-L,L]\times[-L,L]$, discretized as $r_i=ih$ and $z_j=jh$ along the r- and z-axis, respectively, with $i,j=-N,-N+1,\cdots,0,\cdots,N-1,N$ and the mesh width $h=L/N$.

Fig. 2 shows the computational domain. For the electric potential, Dirichlet boundary conditions are imposed at the top (BC4) and bottom (BC3),

$$\phi^+=-E_0\frac{L}{2}\ \text{ at }\ z=L,\qquad \phi^+=E_0\frac{L}{2}\ \text{ at }\ z=-L. \tag{3.1}$$

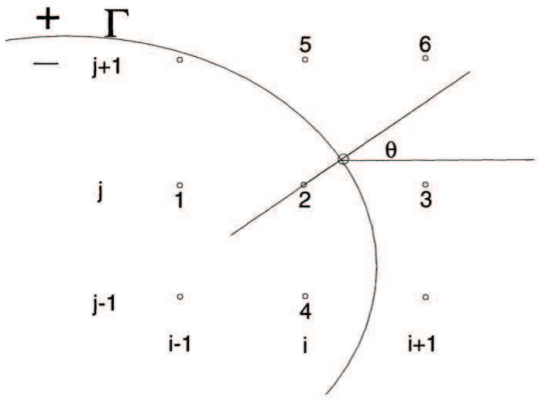

Figure 3: Grid geometry at an irregular point (i,j) from [20].

Neumann boundary condition for the electric field is imposed along the axis of symmetry ($r=0$, BC1) and the side wall ($r=L$, BC2),

$$\frac{\partial \phi}{\partial r}=0 \quad \text{at} \quad r=0 \quad \text{and} \quad r=L. \tag{3.2}$$

For the Stokes equations, boundary conditions for pressure and velocity are specified at $r=0$ (BC1)

$$\frac{\partial p}{\partial r}=0, \qquad \frac{\partial w}{\partial r}=0, \qquad u=0. \tag{3.3}$$

Dirichlet boundary conditions for p, u, and w on the other three sides (BC2-BC4) of the domain are determined from boundary integrals [3]:

$$p=\int\int -\frac{1}{4\pi}\boldsymbol{f}\cdot\nabla\left(\frac{1}{r}\right)dS, \tag{3.4}$$

$$\boldsymbol{u}=\int\int \frac{1}{8\pi\mu}\left(\frac{\delta_{ij}}{r}+\frac{x_i' x_j'}{r^3}\right)f_j dS(x'). \tag{3.5}$$

In the IIM, grid points are classified as regular or irregular points based on their proximity to the interface. A point (i,j) is irregular if its stencil consists of neighbors on either side of the interface, while a regular grid point has its four neighbors on the same side of the interface (see Fig. 3).

3.1 Augmented IIM for the electric potential with axial symmetry

The IIM for a Poisson problem has frequently been utilized to solve Eq. (2.4). For the electric potential we adopt the following general IIM formulation for cases where the net bulk electric charge density (denoted as c in the following equation) is not zero

$$\nabla\cdot(\varepsilon\nabla\phi)=c, \tag{3.6}$$

with boundary conditions at Γ

$$[\![\phi]\!]=\alpha, \qquad [\![\sigma\phi_n]\!]=\beta. \tag{3.7}$$

In our formulation we consider ε to be piecewise constant, therefore Eq. (3.6) can be recast as $\Delta\phi = c/\varepsilon$ in each domain. Moreover, we can use the AIIM (augmented immersed interface method) to solve for the potential, with $[\![\phi_n]\!] = g$ as the augmented variable. First developed as a fast algorithm for elliptic interface problems with discontinuous coefficients [25], the AIIM introduces an unknown function (the augmented variable) to the original set of interface boundary conditions. This augmented variable is solved simultaneously in addition to solution of the elliptic equation. Recently AIIM has been applied to various problems [16, 26], and various modifications have been made to solve the Navier-Stokes equations with piecewise constant fluid viscosity.

The augmented method we use for the electric potential is based on [15], and here we extend it from two-dimensions to three-dimensions with axisymmetry. We use a fixed staggered grid, where the grid points $\mathbf{x}_{ij}$ and potential ϕ_{ij} are defined at the cell center. For the electric potential, the system of Eqs. (3.6)-(3.7) becomes

$$\Delta\phi=\begin{cases} c^-/\varepsilon^- & \text{in } \Omega^-, \\ c^+/\varepsilon^+ & \text{in } \Omega^+, \end{cases} \tag{3.8}$$

with boundary conditions

$$[\![\phi]\!]=\alpha, \qquad [\![\phi_n]\!]=g, \qquad [\![\sigma\phi_n]\!]=\beta. \tag{3.9}$$

We use the standard second-order difference stencil to discretize the Poisson equation on either side of the interface. The finite difference discretization near the interface is modified by the correction term C_{ij}

$$\frac{1}{h^2}\left(\phi_{i+1,j}+\phi_{i-1,j}+\phi_{i,j+1}+\phi_{i,j-1}-4\phi_{i,j}\right)+\frac{1}{2hr_i}\left(\phi_{i+1,j}-\phi_{i-1,j}\right)+\frac{C_{ij}}{h^2}=\bar{c}_{ij}, \tag{3.10}$$

or in matrix form,

$$A\Phi+E\Psi=T. \tag{3.11}$$

Here, Φ and Ψ correspond to ϕ_{ij} and $[\![\phi_n]\!]_{x_k^*}$, respectively, and x_k^* is the orthogonal projection of x at the interface; A is the difference operator, E is the operator acting on the augmented variable, and T is the vector of known solution in the right-hand side. The correction term C_{ij} is non-zero only at irregular grid points (see Fig. 3), and is obtained from performing a Taylor's series expansion about an irregular point on either side of the interface:

$$C_{ij}=[\phi]_{x_k^*}+d[\phi_n]_{x_k^*}+\frac{d^2}{2}\left([\bar{c}_{ij}]-\kappa[\phi_n]-\frac{1}{|\boldsymbol{X}_s|}\frac{\partial}{\partial s}\left(\frac{1}{|\boldsymbol{X}_s|}\frac{\partial[\phi]}{\partial s}\right)\right)_{x_k^*}, \tag{3.12}$$

where d is the signed distance between the irregular grid point and its orthogonal projection $\boldsymbol{x}_k^*$, and κ is the local curvature of the interface. We refer the reader to [15] for detailed derivation of the correction terms, C_{ij}.

At the interface, the relation between $[\![\phi_n]\!]$ and $[\![\sigma\phi_n]\!]$ is expressed by

$$\phi_n^+ + \frac{\sigma^-}{[\![\sigma]\!]}[\![\phi_n]\!] = \frac{[\![\sigma\phi_n]\!]}{[\![\sigma]\!]}, \quad \text{for } \sigma^- > \sigma^+, \tag{3.13}$$

or

$$\phi_n^- + \frac{\sigma^+}{[\![\sigma]\!]}[\![\phi_n]\!] = \frac{[\![\sigma\phi_n]\!]}{[\![\sigma]\!]}, \quad \text{for } \sigma^+ > \sigma^-. \tag{3.14}$$

The choice of Eq. (3.13) or Eq. (3.14) depends on the value of R (=$1/\sigma_r$). This helps ensure that coefficients of $\sigma^{\mp}/[\![\sigma]\!]\mathbf{I}$ are large enough, so that the matrix in Eq. (3.16) is diagonally dominant. We cast Eqs. (3.13)-(3.14) in matrix form, $B^{\pm}\Phi + \sigma^{\mp}/[\![\sigma]\!]\Psi = G$, where B^+ and B^- denote the matrices resulting from the one-sided difference approximation along the normal directions, respectively. The overall linear system becomes

$$\begin{bmatrix} A & E \\ B^{\pm} & \frac{\sigma^{\mp}}{[\![\sigma]\!]}I \end{bmatrix} \begin{pmatrix} \Phi \\ \Psi \end{pmatrix} = \begin{pmatrix} T \\ G \end{pmatrix}. \tag{3.15}$$

We solve Eq. (3.15) by first eliminating Φ to obtain

$$\left(B^{\pm}A^{-1}E - \frac{\sigma^{\mp}}{[\![\sigma]\!]}I \right)\Psi = B^{\pm}(A^{-1}T) - G. \tag{3.16}$$

Eq. (3.16) is a $(N_B+1)\times(N_B+1)$ system. Also, it is one dimension less compared with Eq. (3.15). The electric potential Φ is obtained in three steps: (1) Solve the system $A\Phi^* = T$ for Φ^*; (2) Use GMRES to calculate Ψ from Eq. (3.16); (3) Compute Φ from $A\Phi = T - E\Psi$. We use a fast Poisson solver in steps (1) and (3).

Once we know the potential, we can compute the jump in the Maxwell stress. We use the one-sided least square interpolation [25, 43] to calculate the interfacial potential and electrostatic field. Here, we briefly summarize the one-sided least square interpolation scheme, modified for our axisymmetric case, and the interested readers are referred to [43] for more details. Denoting q the number of grid points used for the interpolation, we derive a system of $q\,(\geq 6)$ equations from the second-order Taylor expansion near the interface

$$\phi(r,z)_q = S_1 + S_2(r-\rho_k)_q + S_3(z-Z_k)_q + S_4(r-\rho_k)_q^2 + S_5(z-Z_k)_q^2 + S_6(r-\rho_k)_q(z-Z_k)_q. \tag{3.17}$$

The problem is cast in matrix form,

$$\zeta \boldsymbol{s} = \boldsymbol{Y}, \tag{3.18}$$

where $\boldsymbol{s} = [S_1, S_2, \cdots, S_6]^T$, $\boldsymbol{Y} = \phi(r,z)_l$, and ζ is the coefficient matrix of relative distances.

The unknown coefficients $\boldsymbol{s}$ is solved using the least square minimization method, where the matrix ζ is expressed as $\zeta = U\Sigma V^*$ by Singular Value Decomposition (SVD). $U_{q\times q}$ and $V^*_{6\times 6}$ are unitary matrices, and

$$\Sigma = \begin{pmatrix} \Sigma_{1,1} & 0 & \dots & 0 \\ 0 & \Sigma_{2,2} & \dots & 0 \\ \vdots & \vdots & \ddots & \vdots \\ 0 & 0 & \dots & \Sigma_{6,6} \\ \vdots & \vdots & & \vdots \\ 0 & 0 & \dots & 0 \end{pmatrix}. \tag{3.19}$$

Eq. (3.18) is then recast as $U\Sigma V^*\boldsymbol{s} = \boldsymbol{Y}$, and we obtain the solution $\boldsymbol{s} = V\Sigma^{-1}U^*\boldsymbol{Y}$. From this calculation, the electric potential and field at (ρ_k, Z_k) are immediately obtained:

$$\phi(\rho_k, Z_k) \approx S_1, \tag{3.20}$$
$$\phi_r(\rho_k, Z_k) \approx S_2, \tag{3.21}$$
$$\phi_z(\rho_k, Z_k) \approx S_3. \tag{3.22}$$

3.2 IIM for the fluid flow field with axial symmetry

For the fluid flow field we use the IIM and adopt the approach developed by Li *et al.* [24] for the incompressible Stokes equations

$$-\nabla p + \mu\Delta\boldsymbol{u} + \boldsymbol{F} = 0, \tag{3.23}$$
$$\nabla\cdot\boldsymbol{u} = 0. \tag{3.24}$$

Eqs. (3.23)-(3.24) are recast as a set of three Poisson equations for the Stokes pressure p, and for components of the Stokes velocity u and w. The divergence of Eq. (3.23) gives

$$\nabla^2 p = \nabla\cdot\boldsymbol{F}, \qquad [\![p]\!] = f_n, \qquad \left[\!\!\left[\frac{\partial p}{\partial n}\right]\!\!\right] = \frac{1}{r}\frac{\partial}{\partial s}(f_\tau r), \tag{3.25}$$

where f_n and f_τ are the components of the boundary force normal and tangential to the interface, respectively. In practice, the singular source term is eliminated from the right-hand side. The pressure satisfies the Laplace equation,

$$\nabla^2 p = 0, \tag{3.26}$$

with specified jump conditions. The standard second-order finite difference discretization gives

$$\frac{1}{h^2}\left(p_{i+1,j} + p_{i-1,j} + p_{i,j+1} + p_{i,j-1} - 4p_{i,j}\right) + \frac{1}{2hr_i}\left(p_{i+1,j} - p_{i-1,j}\right) = C^p_{i,j}, \tag{3.27}$$

where the correction term $C^p_{i,j}$ is determined using the same methodology as in [20]. We solve the resulting system of equations for p, using fast Fourier transforms (FFT). Note that $C^p_{i,j}$ is non-zero only at irregular grid points.

We then compute the velocity field $\boldsymbol{u}=(u,w)$, which is governed by

$$\frac{1}{\mu}\nabla p=\nabla^2\boldsymbol{u}, \tag{3.28}$$

with jump conditions

$$[\![\boldsymbol{u}]\!]=0, \qquad \mu\left[\!\left[\frac{\partial u}{\partial n}\right]\!\right]=f_\tau\sin\theta, \qquad \mu\left[\!\left[\frac{\partial w}{\partial n}\right]\!\right]=-f_\tau\cos\theta. \tag{3.29}$$

We discretize the r-component of velocity to get

$$\frac{1}{h^2}\left(u_{i+1,j}+u_{i-1,j}+u_{i,j+1}+u_{i,j-1}-4u_{i,j}\right)+\frac{1}{2hr_i}\left(u_{i+1,j}-u_{i-1,j}\right)=\pi_{i,j}+C^u_{i,j}, \tag{3.30}$$

where $\pi_{i,j}=\left(p_{i+1,j}-p_{i-1,j}\right)/(2h\mu)$. A similar discretization is obtained for the z-component of $\boldsymbol{u}$. As in the case with p, we obtain solutions for the velocity by FFT [22,24].

The position of the drop interface is updated according to

$$\frac{d\boldsymbol{X}}{dt}(s,t)=(U_\Gamma,W_\Gamma), \tag{3.31}$$

where

$$U_\Gamma=\gamma_1u_{i1,j1}+\gamma_2u_{i2,j2}+\gamma_3u_{i3,j3}-C^U, \tag{3.32}$$

$$W_\Gamma=\delta_1w_{i1,j1}+\delta_2w_{i2,j2}+\delta_3w_{i3,j3}-C^W, \tag{3.33}$$

result from interpolating the Eulerian velocity, $\boldsymbol{u}$ using a second-order interpolation scheme that incorporates the jumps across the boundary [21]. The coefficients γ's and δ's must be determined. In the case of U_Γ, we first choose the three closest points, (r_{i1},z_{j1}), (r_{i2},z_{j2}), and (r_{i3},z_{j3}) to the point (ρ_k,Z_k) on the interface. Then the coefficients γ_k are,

$$\gamma_2=\frac{(z_{j1}-Z_k)(r_{i3}-r_{i1})-(r_{i1}-\rho_k)(z_{j3}-z_{j1})}{(r_{i2}-r_{i1})(z_{j3}-z_{j1})-(r_{i3}-r_{i2})(z_{j2}-z_{j1})}, \tag{3.34}$$

$$\gamma_3=\frac{(z_{j3}-z_{j1})(r_{i1}-\rho_k)-(r_{i2}-r_{i1})(z_{j1}-Z_k)}{(r_{i2}-r_{i1})(z_{j3}-z_{j1})-(r_{i3}-r_{i2})(z_{j2}-z_{j1})}, \tag{3.35}$$

$$\gamma_1=-(\gamma_2+\gamma_3), \tag{3.36}$$

and the correction term

$$C^U=-\left(a_2[u]+a_4[u_r]+a_6[u_z]\right), \tag{3.37}$$

where a_i are linear combinations of the γ_k. u is the r-component of velocity. We use a similar approach to determine the interpolated velocity W_Γ from the z-component of velocity, w. Finally, we advance the markers according to the second-order Adams-Bashforth method

$$\boldsymbol{X}^{n+1} = \boldsymbol{X}^n + \Delta t \left(\frac{3}{2} \boldsymbol{U}_\Gamma^n - \frac{1}{2} \boldsymbol{U}_\Gamma^{n-1} \right). \tag{3.38}$$

3.3 Summary of the numerical algorithm

Prior to solving the governing equations, the system is non-dimensionalized using the following scale: $\mathbf{x} = r_0 \mathbf{x}^*$, $p = \frac{\gamma}{r_0} p^*$, and $\mathbf{u} = U_d \mathbf{u}^*$. Here r_0 is the initial radius of the drop, and U_d is the characteristic velocity. The dimensionless governing equations become (after dropping the *)

$$-\nabla p + Ca \Delta \boldsymbol{u} + \int_0^{2\pi} (\boldsymbol{f}_\gamma + Ca_E \boldsymbol{f}_E) \delta^2 (\boldsymbol{x} - \boldsymbol{X}(s,t)) ds = 0, \tag{3.39}$$

$$\nabla \cdot \boldsymbol{u} = 0, \tag{3.40}$$

$$\nabla \cdot (\varepsilon \nabla \phi) = 0, \quad [\![\phi]\!] = 0, \quad [\![\sigma \phi_n]\!] = 0, \tag{3.41}$$

$$\boldsymbol{E} = -\nabla \phi, \quad \mathbf{M} = \varepsilon \left(\boldsymbol{E}\boldsymbol{E} - \frac{1}{2} E^2 \mathbf{I} \right), \quad \boldsymbol{f}_E = [\![\mathbf{M}]\!] \cdot \boldsymbol{n} \text{ and } \boldsymbol{f}_\gamma = \left(\frac{\rho_s Z_{ss} - \rho_{ss} Z_s}{|\boldsymbol{X}_s|^3} + \frac{Z_s}{\rho} \right) \boldsymbol{n}. \tag{3.42}$$

The electrohydrodynamics thus depends on the capillary number $Ca = \mu U / \gamma$, the electric capillary number $Ca_E = \varepsilon^+ E_0^2 r_0 / \gamma$, and the two ratios ($Q$, R). The capillary number represents the ratio of viscous force to surface tension, and the electric capillary number reflects the strength of the electric field.

Given the position of the drop interface $\boldsymbol{X}^n$ at time t_n, the numerical implementation of the equations proceeds as follows:

1. Compute the electric potential ϕ^n using the augmented IIM described in Section 3.1. With ϕ^n known, use the one-sided least squares interpolation scheme to calculate the interfacial electric field from (3.21) and (3.22). Then use the interfacial electric field to calculate the interfacial electric force, $\boldsymbol{F}_E^n$ from the Maxwell stresses $\mathbf{M}_E^+$ and $\mathbf{M}_E^-$.
2. Compute the interfacial tension force, $\boldsymbol{f}_\gamma$ from (3.42).
3. Using the IIM described in Section 3.2, solve the sequence of three Poisson problems (3.26)-(3.28), for the Stokes pressure and velocity components at time t^{n+1}.
4. Interpolate the fluid velocity to the boundary markers, and update the boundary to its new position $\boldsymbol{X}^{n+1}$.
5. Shift the drop center to the origin $(r,z) = (0,0)$ to off-set the drift of a viscous drop under a DC electric field [10].

As noted in [10] a drop between two parallel plate capacitor (with a fixed jump in electric potential) exhibits a constant drift towards one of the plates. The drift of a viscous drop under a steady electric field is cancelled by an added hydrostatic pressure [10]. Others take advantage of the symmetry with respect to the equatorial plane to reduce the computational domain by half [33,40] (obtaining the solution in only one quadrant of the space). In this work, the drop center is shifted back to the origin at every time step to avoid the drift.

4 Results

4.1 Convergence study

In this subsection, we present the convergence results of our numerical schemes. The computational domain is $(r,z)\in[0,3]\times[-3,3]$, and the mesh size $h=3/N$, where N is the grid number. The permittivity and conductivity ratios are $(Q,R)=(50,0.04)$. We used a time step of $\Delta t=0.001$, and ran the simulations from $t=0$ to $t=0.2$. The number N_B of Lagrangian markers representing the interface scales as $N_B=N/2$.

Table 1 shows the convergence results as the ratio of the solution errors to h^2. We use the solution computed with $N=512$ as the true solution, Y_{exact}, and define $E_\infty=\|Y_N-Y_{exact}\|_\infty/h^2$ and $E_1=\|Y_N-Y_{exact}\|_1/h^2$. The results show that the ratio is approximately constant and non-increasing, which indicates second-order spatial accuracy (similar to results in [23,24]). Another way to determine the accuracy of the numerical method is to define the ratio

$$\text{ratio}=\log_2\left(\frac{\|u_{2N}-u_N\|_\infty}{\|u_{4N}-u_{2N}\|_\infty}\right). \tag{4.1}$$

A ratio around 2 implies second-order accuracy. Table 2 shows the convergence analysis.

Table 1: Mesh refinement results for the velocity components, (u,w,p), and electric potential, ϕ at grid points of the computational domain.

N	$E_\infty(u)$	$E_\infty(w)$	$E_\infty(p)$	$E_\infty(\phi)$	$E_1(u)$	$E_1(w)$	$E_1(p)$	$E_1(\phi)$
32	4.77×10^2	1.59×10^3	2.3×10^3	4.19×10^3	7.27×10^2	8.80×10^2	1.33×10^3	3.79×10^3
64	3.22×10^2	1.05×10^3	1.86×10^3	4.03×10^3	5.49×10^2	5.7×10^2	8.5×10^2	3.69×10^3
128	1.86×10^2	6.62×10^2	1.41×10^3	2.3×10^3	2.38×10^2	3.80×10^2	5.58×10^2	2.13×10^3
256	1.12×10^2	1.7×10^2	8.8×10^2	1.16×10^3	2.34×10^2	1.55×10^2	4.43×10^2	1.17×10^3

Table 2: Mesh refinement results for the velocity components, (u,w,p), and interface position, $\boldsymbol{X}$.

N	$\|u_{2N}-u_N\|_\infty$	ratio	$\|w_{2N}-w_N\|_\infty$	ratio	$\|p_{2N}-p_N\|_\infty$	ratio	$\|\boldsymbol{X}_{2N}-\boldsymbol{X}_N\|_\infty$	ratio
32	3.87×10^{-1}	-	1.29	-	2.00	-	1.99	-
64	6.75×10^{-2}	2.52	2.16×10^{-1}	2.58	3.68×10^{-1}	2.45	7.66×10^{-4}	11.34
128	1.01×10^{-2}	2.74	3.82×10^{-2}	2.5	7.26×10^{-2}	2.34	7.44×10^{-5}	3.36
256	1.71×10^{-3}	2.57	2.59×10^{-3}	3.88	1.34×10^{-2}	2.44	1.06×10^{-5}	2.81

Table 3: Mesh refinement results for the electric potential ϕ at all grid points of the computational domain, and for the interfacial electric potential, ϕ^-, ϕ^+. Results for ϕ^-, ϕ^+ are obtained using the one-sided least squares interpolation.

N	$\|\phi_{2N}-\phi_N\|_\infty$	ratio	$\|\phi^-_{2N}-\phi^-_N\|_\infty$	ratio	$\|\phi^+_{2N}-\phi^+_N\|_\infty$	ratio
32	3.12	-	1.27×10^{-1}	-	1.25×10^{-1}	-
64	8.48×10^{-1}	1.88	3.38×10^{-2}	1.91	3.51×10^{-2}	1.84
128	1.29×10^{-1}	2.72	5.35×10^{-3}	2.66	5.55×10^{-3}	2.66
256	1.77×10^{-2}	2.86	7.12×10^{-4}	2.91	7.39×10^{-4}	2.91

For the interface position, $\boldsymbol{X}=(\rho,Z)$, the errors and rates are averages between components ρ and Z. One can immediately observe that the rate of convergence is second-order for u, w, p and the interface position, $\boldsymbol{X}$.

Table 3 shows the convergence results for the the electric potential values at grid points, and on the interface. We also determine the accuracy of the interfacial electric force by plotting successive errors in the electric force as a function of the grid number, N. Fig. 4 shows the errors between successive grid refinement, $\|(\boldsymbol{F}_E)_{2N}-(\boldsymbol{F}_E)_N\|$, for the interfacial electric force. We observe that the error convergence rate is second-order.

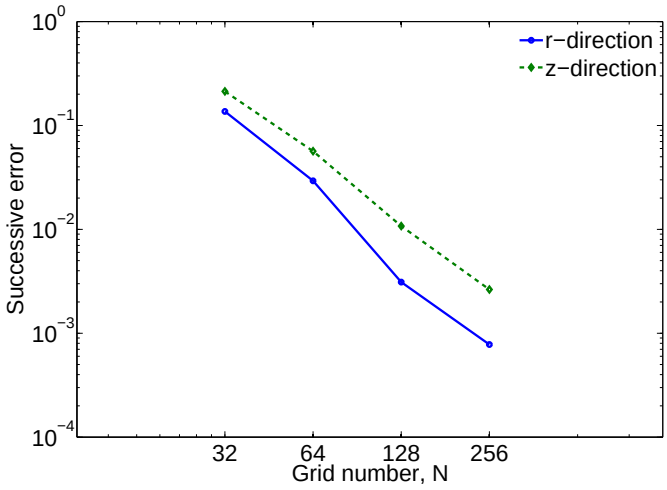

Figure 4: Successive errors for the electric interfacial force ($\boldsymbol{F}_E$) in r (solid curve) and z-direction (dashed curve), as a function of the grid number N. The rate of convergence is nearly second order.

4.2 Equilibrium deformation as a function of conductivity ratio R

In this section we validate our model by comparing to analytical and numerical results in the literature. The equilibrium drop deformation under a DC electric field is quantified

by the deformation number

$$D=\frac{L-B}{L+B}, \tag{4.2}$$

where L and B are the drop size along the major and minor axes, respectively. Depending on the combination of electrical properties of fluids (Q and R, see appendix in [31] and references therein), the equilibrium drop shape under a DC electric field could be either prolate (the major axis is parallel to the electric field and $D>0$), spherical ($D=0$) or oblate (the major axis is orthogonal to the electric field and $D<0$). Moreover there exist two different modes for the prolate shape: one is prolate A with a circulation from the equator to the pole, and the other is prolate B with a circulation from the pole to the equator.

In the limit of small-deformation ($|D|\ll 1$), a first-order approximation is given by Taylor [39]:

$$D\approx\frac{9Ca_E}{16(2+1/R)^2}\left[\frac{1}{R^2}+1-2Q+3\left(\frac{1}{R}-Q\right)\left(\frac{2+3\mu_r}{5+5\mu_r}\right)\right], \tag{4.3}$$

where the ratio of viscosities $\mu_r=\mu^-/\mu^+$. To validate our IIM solver, we perform simulations with varying conductivity ratio (R) and compare our equilibrium drop deformation D against models and and the VOF simulation results as follows.

We use parameters from Tomar *et al.* [41] with $Q=10$. The electric capillary number (equivalent to the Bond number in [41]) is set at $Ca_E=0.18$. Moreover, we fixed $N=128$. The step size is $h=5/N$, and the time step $\Delta t=h/12.5$ (for prolate) and $\Delta t=h/25$ (for oblate). Fig. 5(a) shows a comparison of the numerical simulations with the predictions from Taylor's first-order theory from Eq. (4.3), the spheroidal model of Nganguia *et al.* [31], and results using the volume of fluid (VOF) method in [41]. We note a transition from prolate ($D>0$) to oblate ($D<0$) shapes with increasing R. Results from our IIM simulations are in good agreement with Eq. (4.3) for a small range of R, whereas we observe

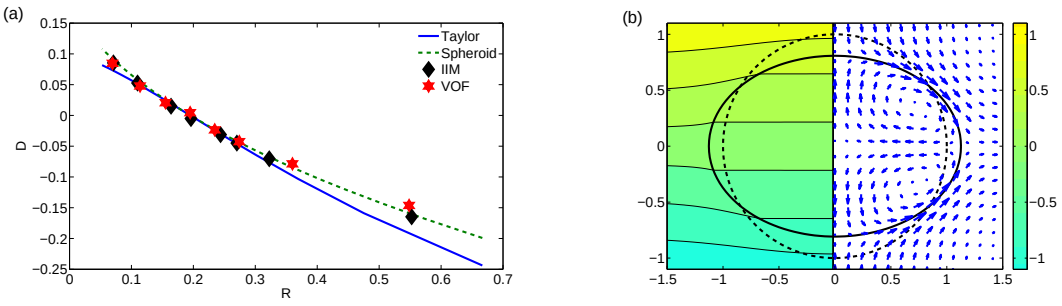

Figure 5: (a) Comparison of the steady state deformation (D) versus conductivity ratio R between Taylor's approximation (Eq. (4.3), solid), the spheroidal model (dashed), the IIM, and VOF results [41]. Other parameters are: $Q=10$, $\mu_r=1$, and $Ca_E=0.18$. (b) Steady state contour plots of the electric potential (left) and circulation plots (right) with $(Q,R)=(10,1/1.81)$ and $Ca_E=0.18$. The dashed curve represents the initially spherical drop shape.

a larger range of R for agreement with our spheroidal model. Fig. 5(b) shows the electric potential (left) and velocity field (right) for $R=0.55$ (an oblate drop with a circulation from pole to equator), where our IIM result is in good agreement with VOF result and the spheroidal model.

4.3 Equilibrium deformation as a function of electric capillary number Ca_E

We simulate drop deformation for various values of the permittivity and conductivity ratios, with parameter values from Fig. 16, Fig. 18 and Fig. 20 of [17]: $(Q,R)=(0.1,0.1)$ for the prolate A drop, $(Q,R)=(2,10)$ for the oblate drop, and $(Q,R)=(50,0.04)$ for the prolate B drop. The spatial resolution is varied between $N=128-512$, with higher resolution needed at electric capillary number $Ca_E \geq 0.25$. The step size is $h=6/N$, and the time step $\Delta t=h/12.5$ (for prolate) and $\Delta t=h/25$ (for oblate). Starting with a spherical drop shape, the simulations are continued until a steady equilibrium shape is obtained.

Fig. 6 shows the equilibrium deformation number versus the electric Capillary number Ca_E for the prolate A and B, and oblate drops in panels (a), (b) and (c), respectively. In addition to results from our IIM simulations, we also superimpose the predictions from the spheroidal model [31], the boundary integral approach [17], and two other analytical models by Taylor [39] and Ajayi [1].

In Fig. 6(a), we observe that for small electric capillary number ($Ca_E \leq 0.05$) all the models and numerical results are in good agreement. This is expected, as all models

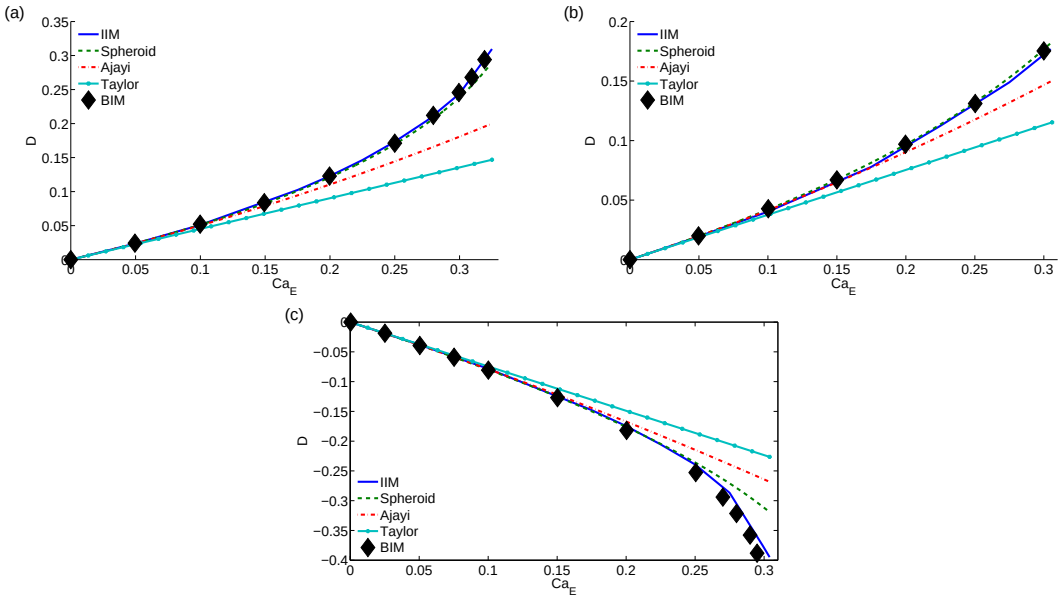

Figure 6: Equilibrium drop deformation versus Ca_E from our IIM (solid), spheroidal model (dashed), Ajayi's second-order approximation (dotted-dashed), Taylor's results (dotted-solid) and the BIM (symbol). (a) Prolate A drop with $(Q,R)=(0.1,0.1)$. (b) Prolate B drop with $(Q,R)=(50,0.04)$. (c) Oblate drop with $(Q,R)=(2,10)$.

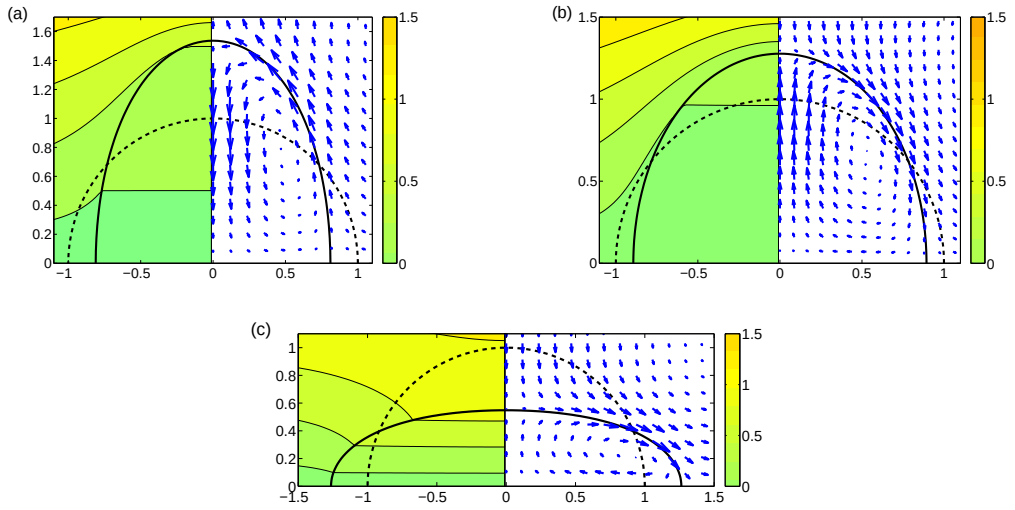

Figure 7: Steady state contour plots of the electric potential (left) and circulation plots (right) for (a) the prolate A drop with $(Q,R)=(0.1,0.1)$ and $Ca_E=0.325$, (b) the prolate B drop with $(Q,R)=(50,0.04)$ and $Ca_E=0.305$, and (c) the oblate drop with $(Q,R)=(2,10)$ and $Ca_E=0.304$. The dashed curve represents the initially spherical drop shape.

should converge to Taylor's result in the limit of small deformation. For $Ca_E>0.05$, Taylor's result start to deviate significantly from the other approximations. Ajayi's second-order model is in good agreement with the spheroidal model and numerical simulations up to $Ca_E\approx 0.1$. The spheroidal model shows excellent agreement with the IIM and BIM simulations for the full range of Ca_E presented in this paper. We make similar observations for the prolate B shape. In Fig. 6(b), Taylor's result is in good agreement with all the other approximations for a larger range of Ca_E values, up to ≈ 0.1. Ajayi's second-order model agrees with the spheroidal and numerical simulations up to $Ca_E\approx 0.2$. For the oblate drop in Fig. 6(c), Taylor's result is in agreements up to $Ca_E\approx 0.1$. Ajayi's result agrees for Ca_E slightly below 0.2, while the spheroidal model matches the numerical results up to $Ca_E\approx 0.225$.

For a 'clean' drop (no surface-active agents such as surfactant on the drop surface) in a DC electric field, Taylor predicted and observed that the circulatory motion is from the equator to the pole (counterclockwise in the first quadrant) for the prolate A drop [39]. On the other hand, a circulation from the pole to the equator (clockwise circulation in the first quadrant) is found inside the prolate B and oblate drops. Fig. 7 shows the steady state drop shape, electric potential, and flow patterns for prolate A and B, and oblate drops. For each panel, the electric potential contour is on the left, while the flow field is depicted on the right.

We also investigate large drop deformation and its dynamics leading to break-up under a strong electric field (large electric capillary number). For large Ca_E the axisymmetric drop shape deviates significantly from spheroids as illustrated in [17]. In partic-

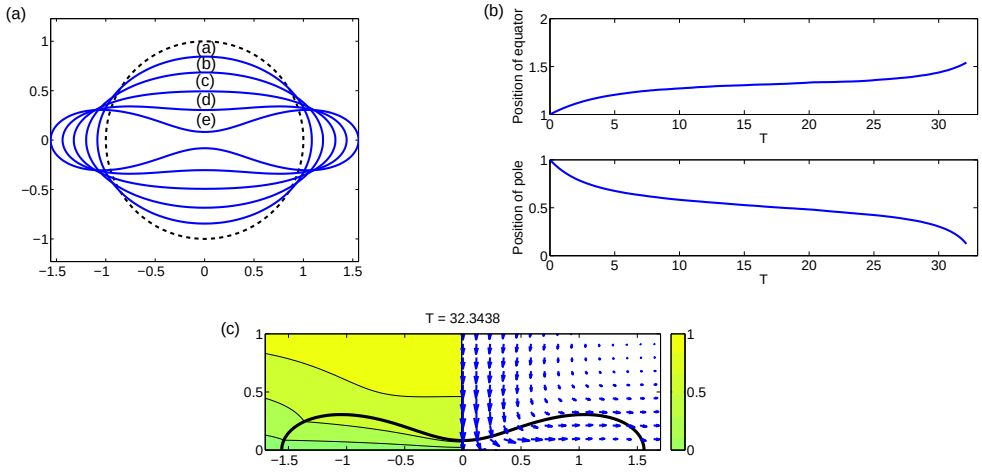

Figure 8: Transient dynamics for the oblate drop in Fig. 6 with $(Q,R)=(2,10)$ and $Ca_E=0.315$. Panel (a): The dashed curve represents the initially spherical drop shape. Time $T=1.4$, 4.7, 18.7, 30, and 32.3 for curve (a), (b), (c), (d), and (e), respectively. Panel (b): Position of the equator (top) and pole (bottom) versus time. Panel (c): Contour plots of the electric potential (left) and circulation plots (right).

ular, there may exist a critical capillary number above which the drop breaks up into smaller droplets. To illustrate that our IIM code captures non-spheroidal drop shape and dynamics leading to drop breakup for large Ca_E, we use the parameters for Fig. 7(c) ($(Q,R)=(2,10)$). Fixing $Ca_E=0.315$ and $N=256$, Fig. 8(a) shows the drop shape at times prior to the pinch-off. This sequence of drop shapes is in good agreement with Fig. 18 in [17], where the boundary integral results show that drop will break up for $Ca_E>0.297$. In addition, our IIM code (with $N=256$) is able to obtain steady spheroidal shapes up to $Ca_E=0.304$, which is slightly higher (by 2.4%) than the threshold 0.297 for break-up reported in [17]. Fig. 8(b) shows the location of the equator (pole) versus time in the top (bottom) panel. The late-time behavior of the pole indicates a pinch-off at the poles around $T\sim 32$. Fig. 8(c) depicts the electric potential contour (left) and flow field (right) at the time before pinch-off.

We also conducted simulations for a prolate A drop with $Ca_E=0.37$ and the same $(Q,R)=(0.1,0.1)$ as those for the prolate A drop in Figs. 6(a) and 7(a). For this set of Q and R, the prolate A drop is predicted to pinch off for $Ca_E\geq 0.34$ [17]. Fig. 9(a) shows the drop shape at times prior to the pinch-off. The electric potential contour and flow field are depicted in Fig. 9(b). We note that, unlike the oblate case in Fig. 8, the prolate A drop takes longer to elongate and get close to pinch-off.

5 Conclusion

In this work we implemented the IIM to simulate the dynamics of a three-dimensional axisymmetric leaky dielectric drop under a DC electric field. Within the leaky dielectric

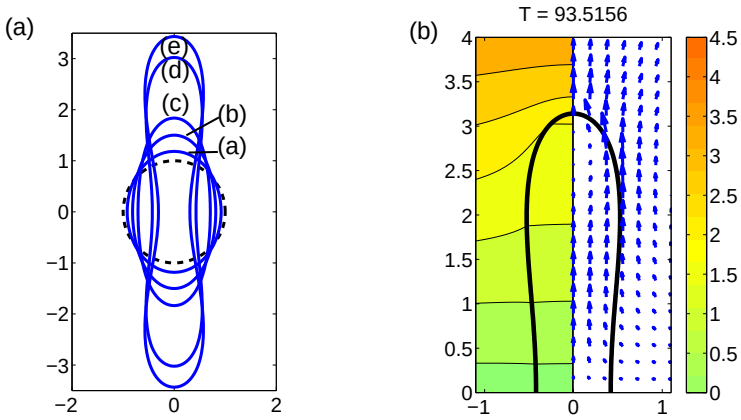

Figure 9: Transient dynamics for the prolate A drop in Fig. 6 with $(Q,R)=(0.1,0.1)$ and $Ca_E=0.37$. Panel (a): The dashed curve represents the initially spherical drop shape. Time $T=3$, 20.3, 50.8, 77.2, and 93.4 for curve (a), (b), (c), (d), and (e), respectively. Panel (b): Contour plots of the electric potential (left) and circulation plots (right).

framework with piecewise constant electrical properties, the electric force is treated as an interfacial force (calculated from the jump in Maxwell stress) along with the capillary force. In this work an IIM solver for the axisymmetric fluid flow [24] is combined with the AIIM solver for the electric field potential [15]. Following the approach in [15], the interfacial electric force is computed from the interfacial Maxwell stress using the one-sided least square interpolation (see Section 3.1). We first performed numerical checks to confirm the second-order convergence of the scheme for the electric potential (at grid points and on the interface), the electric force, and the fluid flow variables. This is a significant improvement from [15], which exhibits first-order convergence due to the immersed-boundary fluid solver. The second-order convergence in our IIM can be improved to higher-order by systematically calculating the higher-order corrections across the interface.

We then ran simulations with different combinations of permittivity and conductivity ratios, and compared against analytical models and boundary integral simulation results. Our results show excellent agreement for a wide range of electric capillary number. Quantitative comparison against the boundary integral simulations from [17] with exactly the same physical parameters shows excellent agreement not only in equilibrium drop deformation and flow pattern, but also the non-equilibrium electrohydrodynamic of a viscous drop.

An obvious advantage of our approach over the boundary integral code is that our IIM code can be easily extended to electro-diffusion in an axisymmetric configuration. In addition, the interface can also be extended to an elastic interface (such as a membrane) for a capsule immersed in a fluid.

Another advantage of our fluid solver is that it can very easily be extended to compute solutions for the incompressible Navier-Stokes equations. In this case, the flow field

variables are decomposed into Stokes (subscript 's'), and continuous (denoted 'c') parts: $\boldsymbol{u}=\boldsymbol{u}_s+\boldsymbol{u}_c$, $p=p_s+p_c$. We obtain the Stokes solutions using the method outlined in Section 3.2, while a projection method is used to compute the continuous solutions $\boldsymbol{u}_c$ and p_c. Interested readers are referred to [3, 23] for more details. We are now using this code to investigate the effects of moderate Reynolds number on electrode formation and electrohydrodynamics of a viscous drop.

Acknowledgments

Y.-N. Young acknowledges support from NSF under grants DMS-1009105 and DMS-1222550. M.-C. Lai acknowledges partial support from the National Science Council of Taiwan under research grant NSC-101-2115-M-009-014-MY3 and NCTS. A. Layton acknowledges support from NSF under grant DMS-126395.

References

[1] O. O. Ajayi. A note on Taylor's electrohydrodynamic theory. *Proc. R. Soc. Lond. A*, 364:499–507, 1978.
[2] N. Aubry. Simple recipe for electroosmotic mixing in microchannels. In K. E. Herold and A. Rasooly, editors, *Lab-on-a-Chip Technology*, pages 201–209. Horizon Scientific Press, 2009.
[3] T. Beale and A. T. Layton. A velocity decomposition approach for moving interfaces in viscous fluids. *J. Comput. Phys.*, 228:3358–3367, 2009.
[4] N. Bentenitis and S. Krause. Droplet deformation in DC electric fields: The extended leaky dielectric model. *Langmuir*, 21:6194–6209, 2005.
[5] P. Brady and O. Desjardins. A sharp, robust, conservative cut-cell immersed boundary technique for stationary and moving structures. In *International Conference on Multiphase Flow*, 2013.
[6] R. K. Dash, T. Borca-Tasciuc, A. Purkayastha, and G. Ramanath. Electrowetting on dielectric-actuation of microdroplets of aqueous bismuth telluride nanoparticle suspensions. *Nanotechnol.*, 18:475711, 2007.
[7] N. Dubash and A. J. Mestel. Behavior of a conducting drop in a highly viscous fluid less conducting than that of the ambient fluid. *J. Fluid Mech.*, 581:469–493, 2007.
[8] J. Q. Feng. Electrohydrodynamic behavior of a drop subjected to a steady uniform electric field at finite electric Reynolds number. *Proc. Math. Phys. Eng. Sci.*, 455:2245–2269, 1999.
[9] J. Q. Feng and K. V. Beard. Three-dimenionsional oscillation characteristics of electrostatistically deformed drops. *J. Fluid Mech.*, 227:429–447, 1991.
[10] J. Q. Feng and T. C. Scott. A computational analysis of electrohydrodynamics of a leaky dielectric drop in an electric field. *J. Fluid Mech.*, 311:289–326, 1996.
[11] J. Fowler, H. Moon, and C. J. Kim. Enhancement of mixing of droplet-based microfluidics. *Proc. IEEE Conf. MEMS*, pages 97–100, 2002.
[12] B. Griffith and C. S. Peskin. On the order of accuracy of the immersed boundary method: higher order convergence rates for sufficiently smooth problems. *J. Comput. Phys.*, 208:75–105, 2005.
[13] J.-W. Ha and S.-M. Yang. Deformation and breakup of Newtonian and non-Newtonian conducting drops in an electric field. *J. Fluid Mech.*, 405:131–156, 2000.

[14] J.-W. Ha and S.-M. Yang. Electrohydrodynamics and electrorotation of a drop with fluid less conducting than that of the ambient fluid. *Phys. Fluids*, 12:764, 2000.
[15] W.-F. Hu, M.-C. Lai, and Y.-N. Young. A hybrid immersed boundary and immersed interface method for electrohydrodynamic simulations. *J. Comput. Phys.*, 282:47–61, 2015.
[16] E. M. Kolahdouz and D. Salac. The Semi Implicit Gradient Augmented Level Set Method. *ArXiv e-prints*, February 2012.
[17] E. Lac and G. M. Homsy. Axisymmetric deformation and stability of a viscous drop in a steady electric field. *J. Fluid Mech.*, 590:239–264, 2007.
[18] M.-C. Lai, C.-Y. Huang, and Y.-M. Huang. Simulating the axisymmetric interfacial flows with insoluble surfactant by immersed boundary method. *Int. J. Numer. Anal. Modeling*, 8:105–117, 2011.
[19] M.-C. Lai and C. S. Peskin. An immersed boundary method with formal second-order accuracy and reduced numerical viscosity. *J. Comput. Phys.*, 160:705–719, 2000.
[20] R. J. Leveque and Z. Li. The immersed interface method for elliptic equations with discontinuous coefficients and singular sources. *SIAM J. Numer. Anal.*, 31:1019–1044, 1994.
[21] R. J. Leveque and Z. Li. Immersed interface methods for Stokes flow with elastic boundaries or surface tension. *SIAM J. Sci. Comput.*, 18:709–735, 1997.
[22] Y. Li. *Numerical methods for simulating fluid motion driven by immersed interfaces*. PhD thesis, Duke University, 2012.
[23] Y. Li, I. Sgouralis, and A. T. Layton. Computing viscous flow in an elastic tube. To appear in *Numer. Math. Theor. Meth. Appl.*
[24] Y. Li, S. A. Williams, and A. T. Layton. A hybrid immersed interface method for driven Stokes flow in an elastic tube. *Numer. Math. Theor. Meth. Appl.*, 6:600–616, 2013.
[25] Z. Li. Fast iterative algorithm for elliptic interface problems. *SIAM J. Numer. Anal.*, 35:230–254, 1998.
[26] Z. Li, M.-C. Lai, G. He, and H. Zhao. An augmented method for free boundary problems with moving contact lines. *Comp. & Fluids*, 39:1033–1040, 2010.
[27] L. C. McConnell, M. J. Miksis, and P. M. Vlahovska. Vesicle electrohydrodynamics in DC electric fields. *IMA J. Appl. Math.*, pages 1–21, 2013.
[28] J. R. Melcher and G. I. Taylor. Electrohydrodynamics: A review of the role of interfacial shear stresses. *Annu. Rev. Fluid Mech.*, 1:111–146, 1969.
[29] Y. Mori. Convergence proof of the velocity field for a Stokes flow immersed boundary method. *Comm. Pure and App. Math.*, LXI:1213–1263, 2008.
[30] Y. Mori and C. S. Peskin. Implicit second-order immersed boundary methods with boundary mass. *Comput. Methods Appl. Mech. Eng.*, 197:2049–2067, 2008.
[31] H. Nganguia, Y.-N. Young, P. M. Vlahovska, J. Bławzdziewcz, J. Zhang, and H. Lin. Equilibrium electro-deformation of a surfactant-laden viscous drop. *Phys. Fluids*, 25:092106, 2013.
[32] S. Nudurupati, M. Janjua, N. Aubry, and P. Singh. Concentrating particles on drop surfaces using external electric fields. *Electrophoresis*, 29:1164–1172, 2008.
[33] H. Paknemat, A. R. Pishevar, and P. Pournaderi. Numerical simulation of drop deformations and breakup modes caused by direct current electric fields. *Phys. Fluids*, 24:102101, 2012.
[34] C. S. Peskin. Numerical analysis of blood flow in the heart. *J. Comput. Phys.*, 25:220–252, 1977.
[35] B. P. Van Poppel, O. Desjardins, and J. W. Daily. A ghost fluid, level set methodology for simulating multiphase electrohydrodynamic flows with application to liquid fuel injection. *J. Comput. Phys.*, 229:7977–7996, 2010.
[36] A. Ramos. *Electrokinetics and electrohydrodynamics in microsystems*, volume 530 of *CISM Inter-*

national Centre for Mechanical Sciences. Springer, 2011.
[37] D. A. Saville. Electrohydrodynamics: The Taylor-Melcher leaky dielectric model. *Annu. Rev. Fluid Mech.*, 29:27–64, 1997.
[38] J. D. Sherwood. Breakup of fluid droplets in electric and magnetic fields. *J. Fluid Mech.*, 188:133–146, 1998.
[39] G. Taylor. Studies in electrohydrodynamics. I. The circulation produced in a drop by electric field. *Proc. R. Soc. Lond. A*, 291:159–166, 1966.
[40] K. E. Teigen and S. T. Munkejord. Influence of surfactant on drop deformation in an electric field. *Phys. Fluids*, 22:112104, 2010.
[41] G. Tomar, D. Gerlach, G. Biswas, N. Alleborn, A. Sharma, F. Durst, S. W. J. Welch, and A. Delgado. Two-phase electrohydrodynamic simulations using a volume-of-fluid approach. *J. Comput. Phys.*, 227:1267–1285, 2007.
[42] O. Vizika and D. A. Saville. The electrohydrodynamic deformation of drops suspended in liquids in steady and oscillatory electric fields. *J. Fluid Mech.*, 239:1–21, 1992.
[43] C. Wang, J. Wang, Q. Cai, Z. Li, H.-K. Zhao, and R. Luo. Exploring accurate Poisson-Boltzman methods for biomolecular simulations. *Comput. Theor. Chem.*, 1024:34–44, 2013.
[44] T. Ward and G. M. Homsy. *Phys. Fluids*, 15:2987–2994, 2003.
[45] H. H. Woodson and J. R. Melcher. *Electromechanical dynamics*. John Wiley and Sons, 1968.
[46] J. Zhang, J. D. Zahn, W. Tan, and H. Lin. A transient solution for vesicle electrodeformation and relaxation. *Phys. Fluids*, 25:071903, 2013.